Instability and rupture of sheared viscous liquid nanofilms

Vira Dhaliwal[1], Christian Pedersen[1], Kheireddin Kadri[2], Guillaume Miquelard-Garnier[2],
Cyrille Sollogoub[2], Jorge Peixinho[2], Thomas Salez[3,*], and Andreas Carlson[1,†]

[1]*Mechanics Division, Department of Mathematics, University of Oslo, 0316 Oslo, Norway*
[2]*Laboratoire PIMM, CNRS, Arts et Métiers Institute of Technology,*
CNAM, 151 boulevard de l'Hopital, Paris, France
[3]*Univ. Bordeaux, CNRS, LOMA, UMR 5798, F-33405, Talence, France*

Liquid nanofilms are ubiquitous in nature and technology, and their equilibrium and
out-of-equilibrium dynamics are key to a multitude of phenomena and processes. We
numerically study the evolution and rupture of viscous nanometric films, incorporating
the effects of surface tension, van der Waals forces, thermal fluctuations, and viscous
shear. We show that thermal fluctuations create perturbations that can trigger film rupture,
but they do not significantly affect the growth rate of the perturbations. The film rupture
time can be predicted from a linear stability analysis of the governing thin film equation,
by considering the most unstable wavelength and the thermal roughness. Furthermore,
applying a sufficiently large unidirectional shear can stabilize large perturbations, creating
a finite-amplitude traveling wave instead of film rupture. In three dimensions, unidirec-
tional shear does not inhibit rupture, as perturbations are not suppressed in the direction
perpendicular to the applied shear. However, if the direction of shear varies in time, then
the growth of large perturbations is prevented in all directions, and rupture can be impeded.

I. INTRODUCTION

Thin liquid films are found in many biological systems such as the human tear film [1,2] as
well as in modern micro- and nanofabrication processes such as multilayer coextrusion of polymers
[3,4]. The stability of liquid films is often an important consideration, with hole formation due to
film rupture often being undesirable [4,5]. In other applications, the rupture and dewetting of thin
liquid films is intended, and can be manipulated to fabricate patterned materials [6,7].

It has been known for over half a century that the rupture of a thin liquid film can be caused
by the amplification of small interfacial perturbations by long-range intermolecular van der Waals
forces. In early works by Vrij [8] and Sheludko [9], the attractive surface interaction due to the
van der Waals forces was represented by a thickness-dependent potential, and thermodynamic
approaches were used to derive a critical wavelength above which perturbations to the flat film
profile are unstable. This potential was later incorporated in a hydrodynamic model, which enabled
derivation of the growth rate of a surface perturbation as a function of its wavelength, thus allowing
the estimation of the rupture time [10].

The hydrodynamic model has been simplified by using the lubrication approximation to derive
the so-called thin film equation, which describes the spatiotemporal evolution of the liquid film
height with a single nonlinear partial differential equation [11,12]. This has led to numerous
analytical and numerical works which have shown that the growth of surface perturbations can be

---

*thomas.salez@cnrs.fr
†acarlson@math.uio.no

024201-1

separated into two regimes: an initial linear regime during which the film height has not yet deviated significantly from its initial value, and a subsequent nonlinear regime during which the growth of perturbations is greatly accelerated [11,13]. Zhang and Lister [14] showed that the nonlinear late-stage dynamics of rupture due to a disjoining pressure are governed by a similarity solution, with the minimum film thickness rapidly decreasing according to a power law. Deviation from an idealized disjoining pressure derived from the Lennard-Jones potential has been shown to produce discretely self-similar solutions, in which the self-similar profile near the rupture point breaks up into smaller self-similar profiles in a fractal-like manner [15]. Such a process was also studied for analogous elastic interfaces [16]. Beyond the initiation of film rupture, thin film models have also been used to describe the droplet patterns formed during dewetting [17].

Van der Waals forces leading to liquid film rupture on solid surfaces only become significant when the film thickness is on the order of tens of nanometers [18]. At these length scales and for common fluids at ambient temperatures, thermally driven molecular motion may cause significant fluctuations of the film height. Thus, it is natural to consider what role these microscopic thermal fluctuations play during the rupture process. To take these into account, a stochastic version of the thin-film equation was derived from the Navier-Stokes equation with an additional random stress tensor [19,20]. This formulation has been used to describe other thin film processes such as the spreading of a viscous bump under an elastic plate [19,21,22] and the transport of solutes through nanopores [23]. Numerical and theoretical studies using the thin film equation with stochastic fluctuations in two dimensions have shown that random thermal fluctuations generate perturbations to an initially flat film profile, which eventually coarsen and approach the wavelength of maximum growth obtained from the linear stability analysis of the fluctuation-free system [24–26]. Simulations have also shown that increasing the fluctuation intensity decreases the rupture time and creates a more nonuniform pattern of droplet sizes after dewetting [25,27,28]. Nevertheless, these thermal effects seem important only at the early stage of the rupture process, with the late-stage behavior being unaffected due to the dominance of the van der Waals force [29].

One way to modify the dynamics of a thin liquid film is by applying a shear flow to it – a situation widely encountered in industrial applications. Interestingly, shear is expected to dampen the amplitude of thermal interface fluctuations [30–32], which might in turn influence the rupture time, i.e., the time it takes for the interface to touch down on the substrate. Numerical studies of thin film rupture without thermal fluctuations in two dimensions have indeed shown that the presence of unidirectional shear can delay rupture when the interface has unstable perturbations [33–35]. To the authors' knowledge, experiments have not yet demonstrated the theorized rupture-suppressing effect of shear, but have shown that shear changes the morphology of the holes created when a polymer film dewets [36].

In this article, we solve numerically the thin film equation with stochastic thermal fluctuations to improve our understanding of how shear affects the rupture dynamics of nanometric liquid films. By studying the film rupture for various combinations of fluctuation intensity, shear rate, and film thickness, we delineate the mechanisms by which rupture is affected in both two dimensions (2D) and three dimensions (3D).

II. MATHEMATICAL MODELING AND NUMERICAL METHODS

A. Thin film equation with thermal fluctuations

We consider the dynamics of a thin viscous liquid film as shown in Fig. 1. The dynamics of the film is represented by the spatiotemporal evolution of its height $h(x, y, t)$. For an initially flat film with height h_0, we define the perturbation to the film height as $\delta h = h(x, y, t) - h_0$. At any point in time, the minimum height of the film is denoted $h_{\min}$. Since we are interested in films where the height $h(x, y, t)$ is much smaller than the horizontal length scale, the viscous flow profile in the fluid layer can be described by the lubrication approximation [37]. A flux balance for a slice of fluid in the film then gives us the thin film equation describing how $h(x, y, t)$ varies with the pressure profile $p(x, y, t)$ [12]. We impose no-slip as a boundary condition at the solid substrate, while noting that a
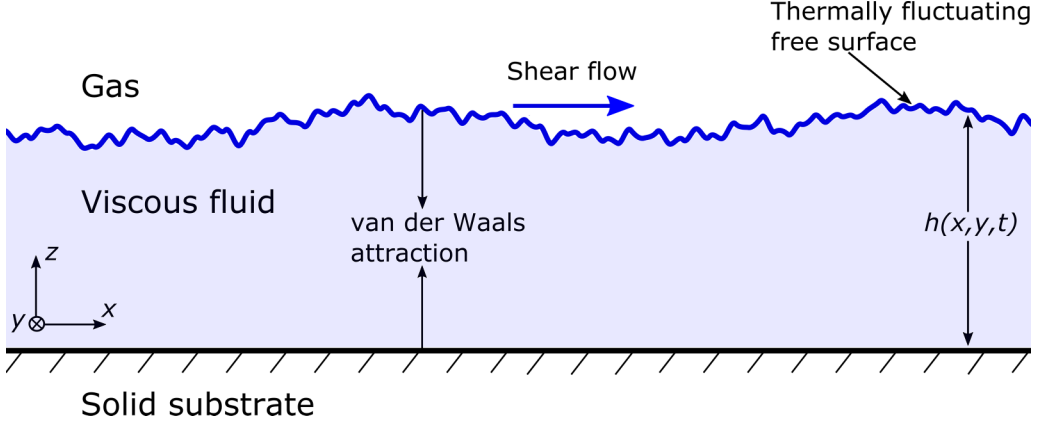
FIG. 1. Schematic of the studied physical system. A thin layer of viscous fluid with thickness $h(x, y, t)$ rests upon a flat solid substrate. A positive disjoining pressure, $\Pi(x, y, t)$, attracts the free surface to the solid substrate. The interface dynamics are also affected by shear and thermal fluctuations. Note that the schematic is not to scale.

finite slip length may play a role at relevant length scales [38]. In our system, the pressure $p(x, y, t)$ has contributions arising from the Laplace pressure due to the curvature of the free surface, the disjoining pressure $A^*/[6\pi h^3(x, y, t)]$ resulting from the van der Waals interactions [39], where A^* is the Hamaker constant, and an additional stochastic stress arising from the thermal fluctuations in the fluid. The shear force is implemented in the tangential stress boundary condition at the film surface, taking the form $\mu \partial \mathbf{u}/\partial z|_{z=h(x,y,t)} = \boldsymbol{\tau}$, where $\mathbf{u}(x, y, z, t)$ is the instantaneous velocity, μ is the dynamic viscosity, and $\boldsymbol{\tau} = \tau \boldsymbol{e}_\tau$ is the specified shear stress at the interface, with magnitude τ and oriented along the unit vector $\boldsymbol{e}_\tau$. Assuming incompressible flow of a Newtonian fluid, small Reynolds number, and small slope of the film profile, $|\nabla h(x, y)| \ll 1$, the thin-film equation reads:

$$0 = \frac{\partial h(x, y, t)}{\partial t} + \nabla \cdot \left[\underbrace{\frac{\gamma}{3\mu} h^3(x, y, t) \nabla \nabla^2 h(x, y, t)}_{\text{Surface tension}} + \underbrace{\frac{A^*}{6\pi \mu h(x, y, t)} \nabla h(x, y, t)}_{\text{van der Waals}} \right.$$

$$\left. + \underbrace{\frac{\tau}{\mu} \boldsymbol{e}_\tau \cdot h(x, y, t) \nabla h(x, y, t)}_{\text{Shear}} + \underbrace{\sqrt{\frac{k_B T}{6\mu}} \nabla \cdot [h^{3/2}(x, y, t) \boldsymbol{\eta}(x, y, t)]}_{\text{Thermal fluctuations}}, \tag{1}$$

where γ is the surface tension coefficient, k_B is Boltzmann's constant, and T is the temperature. The last term in the thin-film equation accounts for the thermal fluctuations in the fluid, where $\boldsymbol{\eta}(x, y, t)$ is a random vector in the (x, y) plane, the two components, η_i with $i = x, y$, of which being independent delta-correlated spatiotemporal Gaussian noises with null averages [19,26], i.e., $\langle \eta_i(x, y, t) \rangle = 0$ and $\langle \eta_i(x, y, t) \eta_j(x', y', t') \rangle = \delta_{ij} \delta(x - x') \delta(y - y') \delta(t - t')$, where δ_{ij} is the Kronecker symbol and δ is the Dirac distribution.

We nondimensionalize Eq. (1) by introducing the scaling relations:

$$h = \bar{h} \sqrt{\frac{A^*}{2\pi \gamma}}, \quad x = \bar{x} \sqrt{\frac{A^*}{2\pi \gamma}}, \quad y = \bar{y} \sqrt{\frac{A^*}{2\pi \gamma}}, \quad t = \bar{t} \sqrt{\frac{9A^* \mu^2}{2\pi \gamma^3}},$$

$$\boldsymbol{\eta} = \bar{\boldsymbol{\eta}} \left(\frac{8\pi^3}{9} \frac{\gamma^5}{A^{*3} \mu^2} \right)^{1/4}, \quad \boldsymbol{\tau} = \bar{\tau} \boldsymbol{e}_\tau \sqrt{\frac{2\pi \gamma^3}{9A^*}},$$

where the bars indicate dimensionless quantities. Both vertical and horizontal lengths are nondimensionalized by a physical length scale, $\sqrt{A^*/(2\pi\gamma)}$, representing the characteristic film thickness at which the disjoining and capillary effects balance. We are mainly interested in the behavior of films with dimensionless initial thickness, $\bar{h}_0 \approx 1$. Films with $\bar{h}_0 \gg 1$ will not be significantly affected by the long-range van der Waals forces, while films with $\bar{h}_0 \ll 1$ will rupture almost instantaneously. To ensure the validity of the lubrication approximation while using this scaling, the nondimensional horizontal domain size $\bar{L}$ is always much larger than $\bar{h}$. The time is normalized by the aforementioned length scale divided by the capillary velocity $\gamma/(3\mu)$. The dimensionless thin film equation with thermal fluctuations thus reads:

$$0 = \frac{\partial h(x,y,t)}{\partial t} + \nabla \cdot \left[h^3(x,y,t)\nabla\nabla^2 h(x,t) + \frac{1}{h(x,t)}\nabla h(x,y,t) \right]$$
$$+ B\boldsymbol{e}_\tau \cdot h(x,y,t)\nabla h(x,y,t) + Q\nabla \cdot [h^{3/2}(x,y,t)\boldsymbol{\eta}(x,y,t)], \tag{2}$$

where we have dropped the bars for simplicity, and introduced two dimensionless numbers:

$$B = \bar{\tau} = \tau\sqrt{\frac{9A^*}{2\pi\gamma^3}}, \tag{3}$$

$$Q = \sqrt{\frac{\pi k_B T}{A^*}}, \tag{4}$$

representing the dimensionless shear force, and the dimensionless thermal roughness (or the ratio between thermal and disjoining energies), respectively. Along with the initial film height h_0, these parameters define the thin-film dynamics. Although a wide range of values for these parameters can be imagined in various scenarios, we focus on the widely studied case of polystyrene (PS)/polymethylmetacrylate (PMMA) multilayers, for which it has been shown that optimized extrusion conditions can lead to continuous layers as thin as 20 nm [4]. Typical values for extrusion temperature, surface tension, dynamic viscosity and Hamaker constant can be set to 220°C, 1 mN/m [40], 10 000 Pa s [4], and 2×10^{-18} J [35,41], respectively. In this case, the thermal roughness at the interface has an amplitude $\sqrt{k_B T/\gamma} \approx 2.5 \times 10^{-9}$ m, and $Q \approx 10^{-1}$ which is in the upper range of the values presented in this study, while h_0 is around 1.1 for a 20 nm layer. For such films, shear rates of up to 100 s^{-1} are possible, meaning that B can take values up to around 50 [42].

We note that, when we model thin films in 2D (i.e., when there is invariance in the y direction), the fluctuation vector $\boldsymbol{\eta}$ needs to be adapted due to the inherently three-dimensional nature of thermal fluctuations. Equation (2) remains valid, but $\boldsymbol{\eta}(x,t)$ is now a random vector in the x direction only, the single component η of which being spatiotemporal Gaussian noise with $\langle\eta(x,t)\rangle = 0$ and $\langle\eta(x,t)\eta(x',t')\rangle = \delta(x-x')\delta(t-t')$. As a consequence, Q is modified in 2D, as

$$Q_{\text{2D}} = \sqrt{\frac{\pi k_B T}{\bar{w}A^*}}, \tag{5}$$

where $\bar{w} = w\sqrt{\frac{2\pi\gamma}{A^*}}$, with w a new length scale representing the width in the y direction. The effect of the finite width of a narrow film is thus simply to modify the parameter Q_{2D}.

B. Finite-element solver

We solve the dimensionless thin film equation with thermal fluctuations [Eq. (2)] using the finite-element method. In all numerical solutions, the initial condition is a flat film with dimensionless thickness h_0. Both in 2D and 3D, periodic boundary conditions are imposed in the horizontal directions.

To solve Eq. (2), the order of the partial differential equation is first reduced by introducing the linearized film curvature $\nabla^2 h(x,y,t)$ as a separate variable. Equation (2) then simplifies to a system of two coupled second order partial differential equations. These are then expressed in

weak form where boundary terms disappear due to the periodic boundary conditions. The scalar fields $\nabla^2 h(x, y, t)$ and $h(x, y, t)$ are discretized with linear elements and solved using a Newton solver from the FEniCS library [43]. For the 2D case, the numerical solutions are realized on the domain $x = [0, 65]$ with an equidistant grid spacing $\Delta x = 0.32$. In the 3D case, the domain is $x \times y = [0, 64] \times [0, 64]$, discretised into a triangular grid with spacings $\Delta x = \Delta y = 0.16$ for solutions used to generate the contour plots. For the data shown in other figures where many iterations are averaged, the grid spacing is increased to $\Delta x, \Delta y = 0.64$ to shorten the computational time, and we have checked that the results are insensitive to the change in spatial resolution. Due to the fact that Eq. (2) involves a traveling wave, an implicit second-order Crank-Nicholson scheme is required for numerical integration to prevent numerical dispersion for large values of B. The size of the time step for all solutions shown is $\Delta t = 0.003$, with the exception of certain solutions involving $B > 30$ as well as the adaptive time step solutions described later in this section and in Appendix A.

The stochastic term requires us to impose a new random vector $\boldsymbol{\eta}(x, y, t)$ at every nodal point for each timestep. $\boldsymbol{\eta}(x, y, t)$ is implemented in python by assigning random numbers using the "normal" function in the "random" class of NUMPY, which generates pseudorandom numbers using the Mersenne Twister [44]. The values are drawn from a Gaussian distribution with zero mean and a variance of $1/(\Delta x \Delta t)$ in 2D and $1/(\Delta x^2 \Delta t)$ in 3D. At every time step, each component of $\boldsymbol{\eta}(x, y, t)$ is assigned a new value at every point in the mesh. Due to the stochastic nature of $\boldsymbol{\eta}(x, y, t)$, the film dynamics and rupture time vary somewhat between individual numerical solutions, despite all the input parameters being identical. To obtain statistically robust results for the wavelength and rupture time, we repeat the computations and average the results $N = 20$ times for 2D solutions and $N = 5$ times for 3D solutions. Nevertheless, the variance of the rupture time and wavelength is generally so small that the trends we describe can be observed even for a single run.

For the simulations of the fluctuation-free version of Eq. (2), an initial sinusoidal perturbation of amplitude $\delta h_0 = 0.001$ is imposed. To maintain the periodic boundary condition, the extent of the domain, L, is set to eight times the wavelength of the perturbation.

Previous works on shear-free films as well as the initial simulations of our system indicate that the highly nonlinear van der Waals force is completely dominant during the final stage of rupture when the minimum film height $h_{\min}(t) = \min(h(x, y, t))$ approaches zero [14,29]. Due to the accelerated dynamics in this regime, a much smaller time step is required to capture the final moments before film rupture. To address this, we compute solutions with an adaptive time step, the results of which are shown in Appendix A. In those computations, the time step starts at $\Delta t = 0.1$ but is gradually reduced as rupture accelerates, reaching a minimum value of $\Delta t \approx 10^{-8}$. The grid spacing is also decreased to $\Delta x = 0.001$ to resolve more of the details near the rupture point. As shown in Appendix A, we recover the expected $h_{\min} \sim (t_R - t)^{1/5}$ power law of Zhang and Lister [14], and also observe that although this stage of rupture accounts for only a tiny fraction of the total duration of the film dynamics until rupture, it makes up most of the computational time due to the reduction in the time step. Our solutions with the adaptive timestep also show that the late stage before rupture seems to be independent of the thermal fluctuations and shear. We also note that close to rupture, lubrication theory cannot be used to describe the local flow [45]. Since we are mainly interested in understanding the instability growth rather than the details in the already characterized final instants before rupture, we decide to fix the time step and stop the numerical algorithm when $h_{\min}$ reaches an arbitrary threshold $h^* = 0.33$, which ensures that we capture the early-stage dynamics without using unnecessary computational resources. We denote the time at which this occurs as the rupture time t_R.

C. Linear stability analysis

From the numerical solution of Eq. (2), as will be described below, it is clear that the thermal fluctuations only play a major role in the evolution of $h_{\min}$ during the first few time steps. As shown in Appendix A, it is also clear that the late stage of pre-rupture film dynamics, when $h_0 - h_{\min} \gg 0.1$, is very short and as such does not make a significant contribution to the measured rupture

time. Thus, we presume that the rupture time of the film is primarily determined by how quickly perturbations grow while they are still too small for nonlinearities to dominate. Here, we perform a linear stability analysis on the fluctuation-free version of Eq. (2) (i.e., with $Q = 0$) [34,35]. We introduce a small sinusoidal perturbation to an initially flat film, of the form

$$h(x, t) = h_0 + h'e^{ikx+\omega t}, \tag{6}$$

where k is the dimensionless angular wave number, ω is the dimensionless complex growth rate, and h' is the amplitude of the perturbation with $h_0 \gg h'$. Inserting Eq. (6) into the fluctuation-free version of Eq. (2) and linearising the equation gives us the following dispersion relation

$$\omega = \left(\frac{k^2}{h_0} - k^4 h_0^3\right) - ikBh_0, \tag{7}$$

with growth rate $\frac{k^2}{h_0} - k^4 h_0^3$ and wave speed Bh_0. From Eq. (7), we expect that the effect of the shear within the linear regime is simply to cause a horizontal translation in the direction of shear with speed Bh_0. Moreover, only perturbations with a wavelength above a critical wavelength $\lambda_c = 2\pi h_0^2$ will grow in time, and the fastest growing mode has dimensionless wavelength

$$\lambda_d = 2\pi\sqrt{2}h_0^2. \tag{8}$$

The growth rate associated with this dominant wavelength is

$$\omega_d = \frac{1}{4h_0^5}. \tag{9}$$

Presuming that the fluctuations trigger perturbations across the wavelength spectrum, we expect that the mode of wavelength λ_d will be the dominant mode observed in our numerical results, and thus govern the change in minimum height of the film. If we only consider the minimum height in Eq. (6), presume that the growth rate of this corresponds to Eq. (9), and divide by h_0, then we get the following expression for how the minimum height of the film varies with time:

$$\frac{h_{\min}(t)}{h_0} = 1 - \frac{h'}{h_0}e^{\omega_d t}. \tag{10}$$

We consider rupture to occur at the time t_R when $h_{\min}$ reaches an arbitrary threshold value, $h^* = 0.33$, at which the van der Waals forces become dominant:

$$\frac{h^*}{h_0} = 1 - \frac{h'}{h_0}e^{\omega_d t_R}. \tag{11}$$

Solving this equation for t_R and inserting our expression for the dominant growth rate in Eq. (9), we then obtain the following estimate for the film rupture time:

$$t_R = 4h_0^5 \ln\left(\frac{h_0 - h^*}{h'}\right). \tag{12}$$

III. RESULTS AND DISCUSSION

A. Two-dimensional case

An example of the numerical solution of Eq. (2) without shear ($B = 0$) in 2D is shown in Fig. 2(a) in the form of height profiles along x at different times. Thermal fluctuations eventually give rise to sinusoidal-like perturbations with a certain wavelength, which then grow until the film ruptures. For each film height h_0, the wavelength of the unstable film profile that develops closely matches the dominant wavelength λ_d predicted in Eq. (8) and the rate of change of $h_{\min}(t)$ closely matches the value predicted by Eq. (9).

In Figs. 2(b) and 2(c), we can see how $h_{\min}$ changes in time during individual numerical solutions for different values of Q. As discussed above, Q is proportional to the dimensionless thermal
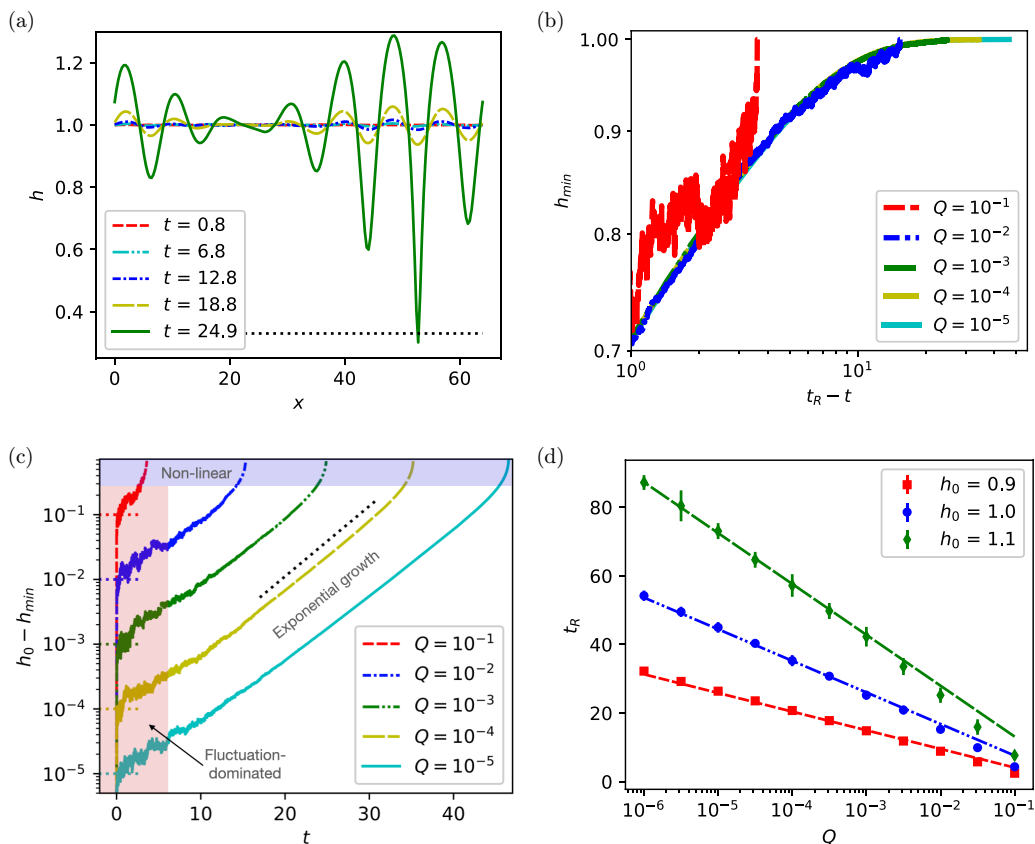
FIG. 2. (a) Profiles of an unstable 2D thin film with $Q = 10^{-3}$, $B = 0$, and $h_0 = 1$ at various times. We stop the numerical algorithm when the minimum film height $h_{\min}$ reaches an arbitrary threshold value $h^* = 0.33$ (represented by the dotted black line), as described in Sec. III A. (b) Time evolution of the minimum film height, $h_{\min}$, plotted for solutions with initial height $h_0 = 1.0$ and different fluctuation intensities, Q. (c) Amplitude of the height perturbation as a function of time for the same simulations. The dotted black line has a slope corresponding to the prediction of Eq. (10) with arbitrary amplitude. The coloured dotted lines on the left indicate the value of Q corresponding to each solution. The three regimes mentioned in the text have been identified by eye as follows: the fluctuation-dominated regime at the beginning of the solutions has been shaded red, while the area shaded in blue represents the nonlinear regime at the end of the solution. (d) Mean rupture time t_R of a film with $B = 0$ as a function of Q for different values of h_0. The dashed lines represent Eq. (13) with no free parameter for each value of h_0. Error bars represent the standard deviation for a set of $N = 20$ numerical solutions for each data point.

roughness, and we here present results as Q varies from relatively small values until the limit where thermal fluctuations are so large that they rapidly cause rupture even without a disjoining pressure. Our results show that the primary effect of thermal fluctuations is to instigate a perturbation of a characteristic size Q during the first time steps. For $Q \gtrsim 10^{-2}$, these fluctuations are strong enough to almost immediately initiate the nonlinear rupture of the film. For smaller values of Q, however, fluctuations with size approximately Q naturally continue to occur at all times, but after $t \approx 10$, the minimum height begins to decrease exponentially as one would expect in the fluctuation-free case, and the fluctuations become insignificant in comparison to the growing sinusoidal perturbation. In fact, turning the fluctuations off after the minimum height has entered this exponential phase does not alter the rupture time. As shown in Fig. 2(b), the time evolution of $h_{\min}$ as the film

approaches rupture is almost identical for different values of Q; the strength of the fluctuations seems to only determine how far back in time from the moment of rupture the curve starts at. In Fig. 2(c) one can also see quite clearly that there are three distinct regimes during rupture: first a fluctuation-dominated phase that initiates a perturbation [shaded red in Fig. 2(c)], then a period of exponential growth of the roughly sinusoidal perturbation [unshaded in Fig. 2(c)], followed by a phase where the growth toward rupture is greatly accelerated due to the nonlinear effects of the disjoining pressure term in Eq. (2) [shaded blue in Fig. 2(c)]. The predominance of the exponential growth period during the rupture process seen in Fig. 2(c) suggests that the rupture time of a film can be predicted by Eq. (12). We also see from Fig. 2(c) that the initial perturbation size, h', is approximately equal to Q. Setting $h^* = 0.33$, which appears to be a reasonable bound of the linear domain (i.e., with exponential growth of the instability), we can rewrite Eq. (12) as

$$t_R = 4h_0^5 \ln \left(\frac{h_0 - 0.33}{Q} \right). \tag{13}$$

In Fig. 2(d) we present the numerically measured rupture time from repeated numerical solutions of our system as a function of Q for various values of h_0. The predicted rupture time from Eq. (13), represented by the straight dashed lines, provides an excellent fit to the data with no adjustable parameters, as long as the fluctuations are small enough for the exponential growth regime to be significant (i.e., $Q \lesssim 10^{-2}$). We note that the dynamics of thicker films with strong thermal fluctuations are expensive to resolve using our formulation, but their rupture times have recently been described using rare-event theory [46]

We now turn our attention to the effects of shear on the previous phenomenology. Equation (2) is simulated with $B \neq 0$ and solutions are stopped either at rupture when $h \leqslant 0.33$, or when the simulation has reached a maximum time of $t = 100$. In Figs. 3(a)–3(c), we see snapshots of the film profile under shear with three different values of B. As predicted by the linear stability analysis (Sec. II C), the constant shear term leads to a simple horizontal translation of the perturbation in the shear direction, with speed Bh_0. We observe that the perturbations remain roughly sinusoidal-like during the exponential growth stage, and maintain a wavelength close to λ_d as well as a growth rate of approximately ω_d. In the nonlinear regime, however, they start to deform as the van der Waals forces become stronger, which gives rise to characteristically slanted asymmetric shapes in the nonlinear stage. For $B \gtrsim 5$, the change in shape is noticeable, and is associated with a short period of decreased perturbation growth, which leads to a slight increase in rupture time, as shown in Figs. 3(a) and 3(d). As shear is increased to $B \gtrsim 11$, as can be seen in Figs. 3(b) and in Fig. 3(d), the perturbations begin to stabilize when they reach a certain size, and a stable wave seems to form for a period of time, before it eventually ruptures. For shear stronger than a critical value of $B \approx 12.5$, this stable translating perturbation does not rupture within the computational time. We denote this critical value as B_{crit}. For $B > B_{\text{crit}}$, the perturbation waveform seemingly propagates indefinitely as shown in Figs. 3(c) and 3(d).

In Fig. 3(d) it is apparent that imposing a shear below B_{crit} can delay rupture to some extent. This effect is quantified in Fig. 4(a), where it can be seen that imposing $B > 5$ leads to a modest increase in rupture time, and that this effect is dramatically increased as B approaches B_{crit}. Figure 3(d) also suggests that beyond B_{crit}, the amplitude of the stable traveling wave generated under shear is dependent on the size of B. This is indeed the case, as is shown in Fig. 4(b). Just above B_{crit}, the minimum height of the final film profile is around $h_{\text{min}} = 0.65$, but this increases as B is increased, eventually converging towards a complete suppression of the perturbation as B approaches infinity.

Interestingly, we note that the observed value of $B_{\text{crit}} \approx 12.5$ is larger than the value of 9.7 observed for the fluctuation-free case with an initial perturbation of wavelength λ_d by Davis *et al.* [34]. To understand why this is the case, we solve the fluctuation-free analog of our thin film equation (i.e., Eq. (2) with $Q = 0$ and a sinusoidal initial perturbation [35]) for various perturbation wavelengths and values of B. In Fig. 4(c) we plot the resulting increase in rupture time with B for a few different values of λ. In this plot we note that the critical shear for the dominant mode of wavelength λ_d is indeed around 9.7, but that larger and smaller wavelengths require more shear to
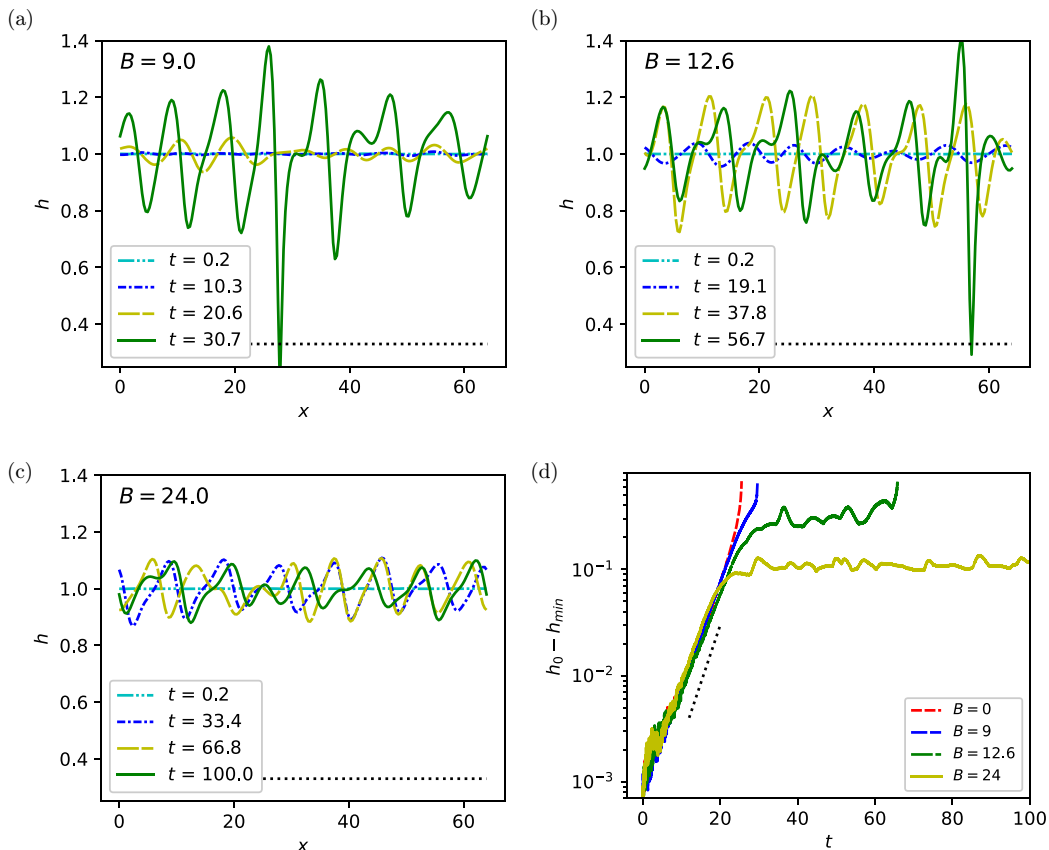
FIG. 3. (a)–(c) Profiles of sheared 2D thin films with $Q = 10^{-3}$ and $h_0 = 1$ at different times. The shear is from left to right in each case, with a nondimensional size B specified at the top of each figure. The dotted black line at the bottom indicates the threshold value $h^* = 0.33$ at which the numerical algorithm is interrupted. (a) $B = 9.0$, (b) $B = 12.6$, (c) $B = 24.0$, (d) time evolution of the height perturbation $h_0 - h_{\min}(t)$ for $Q = 10^{-3}$, $h_0 = 1$, and different values of dimensionless shear stress B. The dotted black line indicates an exponential behavior as predicted by Eq. (10).

suppress rupture. We propose that fluctuations enable rupture even beyond the critical shear of the dominant mode by triggering secondary modes once the dominant mode begins to stabilize. This is supported by the fact that the critical shear observed when fluctuations are present approximately matches the largest values of B_{crit} for large and small wavelengths, as is shown in Fig. 4(d).

In Fig. 3, we observe that the initial perturbation in film height, $h_0 - h_{\min}(t = \Delta t)$, due to the stochastic term seems to be of size Q regardless of the strength of the shear. This is rather unexpected [31] if the size of the initial perturbation is interpreted as the equilibrium thermal roughness. We note however, that the sinusoidal perturbations that lead to rupture form within the first few time steps of the computation, long before the interface settles to an equilibrium roughness. This is discussed in more detail in Appendix B, where we also show that the equilibrium thermal roughness is decreased by B when there is no disjoining pressure.

B. Three-dimensional case

Although our results in two dimensions shed light on 2D film rupture, it is not clear how these effects translate to physically realistic 3D films. To quantify the effect of spatial dimensions, we
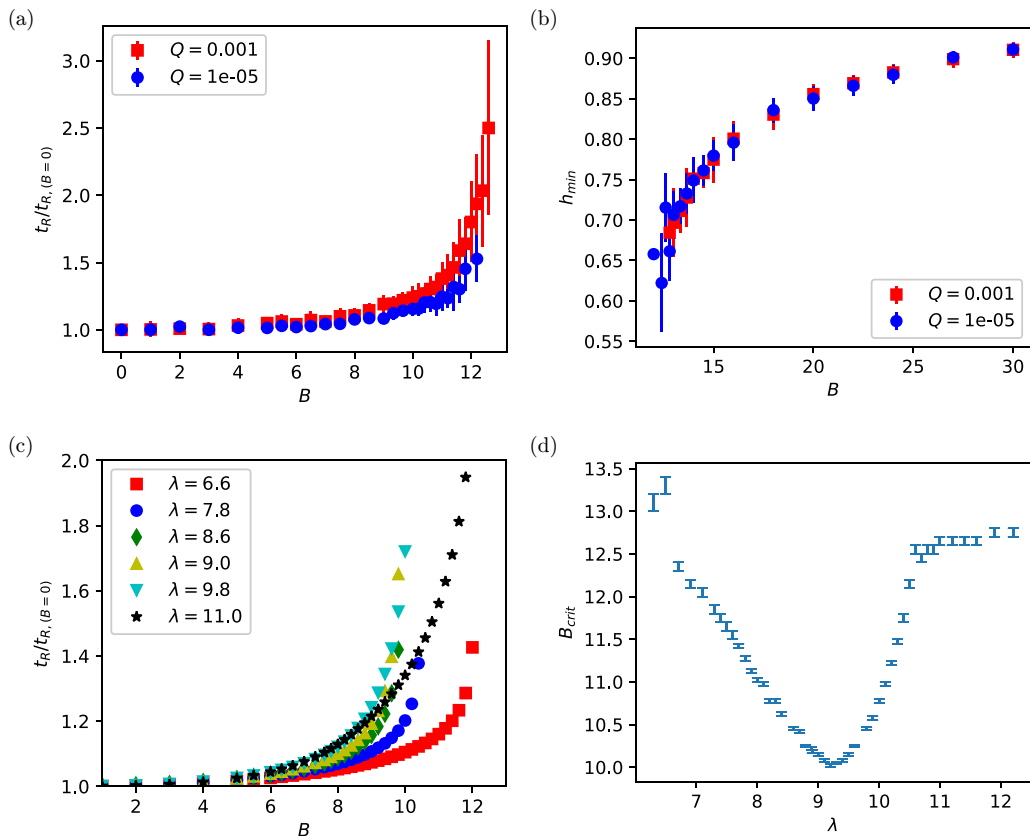
FIG. 4. (a) Rupture time t_R as a function of B for two different values of Q. Rupture times are normalized by the rupture time for $B = 0$. Error bars represent the standard deviation for a set of 20 numerical solutions for each data point. (b) Final value of the minimum film height as a function of B for values above B_{crit}. Error bars represent the standard deviation for a set of 20 numerical solutions for each data point. (c) Rupture time as a function of B for fluctuation-free thin films with initial perturbations of varying wavelength λ. (d) Plot of the critical shear required to suppress rupture within the simulated time period as a function of λ. The top and bottom of the error bars show the lowest shear that did not rupture and the largest shear that did rupture, respectively.

solve Eq. (2) to obtain 3D film profiles, obtaining the results shown in Fig. 5. In Figs. 5(a)–5(c), we note that the shear-free rupture process is both qualitatively and quantitatively similar to the observations in two dimensions [see Fig. 2(a)]: the stochastic fluctuations give rise to small perturbations that coarsen until a characteristic size given by λ_d and subsequently grow over time. The surface depressions that lead to rupture have a circular-like cross-section, but grow with the same growth rate as in the 2D case [Eq. (9)]. The rupture time is still fairly well described by Eq. (12).

In Figs. 5(d)–5(f) (as well as in the supplemental video [47]), we can see how a strong unidirectional shear in the y direction affects the three-dimensional film rupture process. In this case, the shear force has a suppressing effect on perturbations along the shear direction, but perturbations grow freely in the transverse direction. As the perturbations grow to a significant size, they begin to align with the direction of shear, and eventually form a clear pattern of ridges. These ridges then deepen as the film rupture process proceeds. In Fig. 6(a), we show how the minimum film height evolves in time for 3D solutions of rupture with unidirectional shear of varying strength. As in the 2D case, the growth rate in the exponential regime is close to ω_d predicted by the linear stability analysis. In contrast to the 2D case of Fig. 3, however, unidirectional shear does not prevent rupture
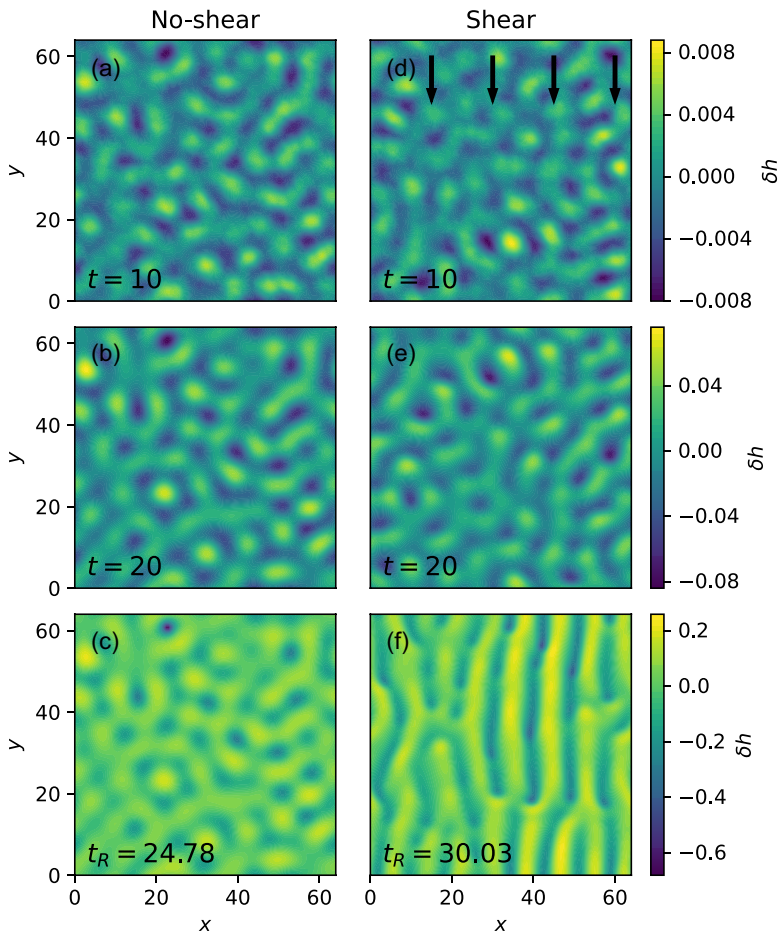
FIG. 5. Contour plots illustrating the height $h(x, y, t)$ of 3D thin films for different times, with $Q = 10^{-3}$. The color represents the deviation $\delta h(x, y) = h(x, y) - h_0$ from the initial film thickness h_0. (a–c) No-shear ($B = 0$) case, where (c) shows the final time step at which the film ruptures. (d–f) Shear ($B = 30$, along y axis) case, where (f) shows the final time step at which the film ruptures. Note that the direction of shear [as indicated by the black arrows in panel (d)] is not the same as in Fig. 1.

from occurring in a 3D film. Nevertheless, for $B > B_{\text{crit}}$ there is a small increase in rupture time, as shown in Fig. 6(b), caused by the fact that the perturbations need to rearrange themselves when they are suppressed in the shear direction.

Since the film rupture time is weakly affected by unidirectional shear at the interface, we then attempted to impose a rotating shear stress, as was done previously by Davis *et al.* [34]. To do so, Eq. (2) is again solved numerically, but the direction of the shear force, $\vec{e}_\tau$, is now varied sinusoidally in time with an angular frequency Ω. The resulting rupture process can be seen in Fig. 7 (as well as in the supplemental video [47]), and is further analyzed in Fig. 8. During the linear regime, the perturbations rotate as the direction of $\vec{e}_\tau$ changes, but grow with the same growth rate as they would have without shear. Once the perturbations become big enough for nonlinear effects to emerge, the perturbations begin to be suppressed in the direction of shear, leading to a reorientation as in the unidirectional case. For very small frequencies, $\Omega \ll 2\pi/t_{R,B=0}$, the change in direction is too slow to affect the rupture process significantly. When Ω is increased, however, the shear has time to switch directions and suppress the perturbations that have grown in the initially cross-shear direction. This leads to periodic reorientation of the perturbation profile with an angular
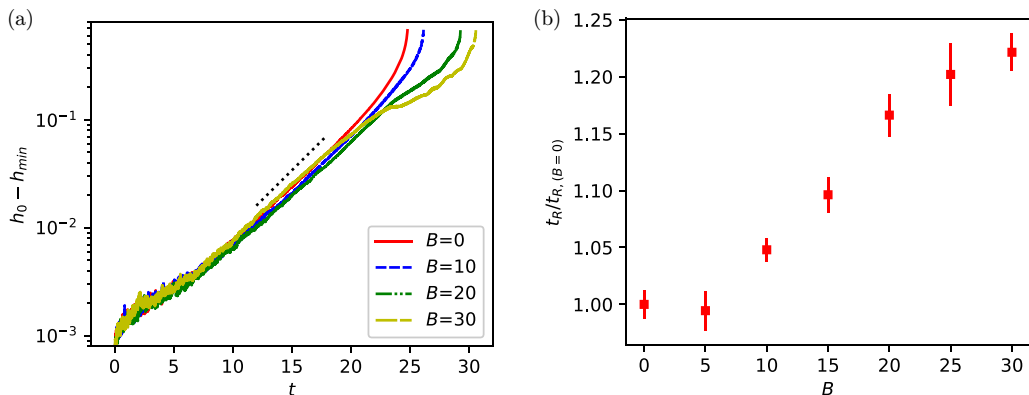
FIG. 6. (a) Time evolution of the height perturbation $h_0 - h_{\min}(t)$ for different values of B in 3D solutions, with unidirectional shear and for $Q = 10^{-3}$, $h_0 = 1$. The dotted black line line indicates exponential behavior with a growth rate given by Eq. (9). (b) The rupture time as a function of shear magnitude, where the error bars represent the standard deviation for a set of five numerical solutions for each value of B.

frequency equal to Ω, and an overall delay of rupture. For rapidly rotating shear, the perturbations remain essentially circular in cross-section and resemble the perturbations seen in the shear-free case shown in Figs. 5(a)–5(c). If B is sufficiently large, and Ω has an appropriate value, then the perturbation can be completely suppressed until the maximum computational time of 50, as is the case in Fig. 7.
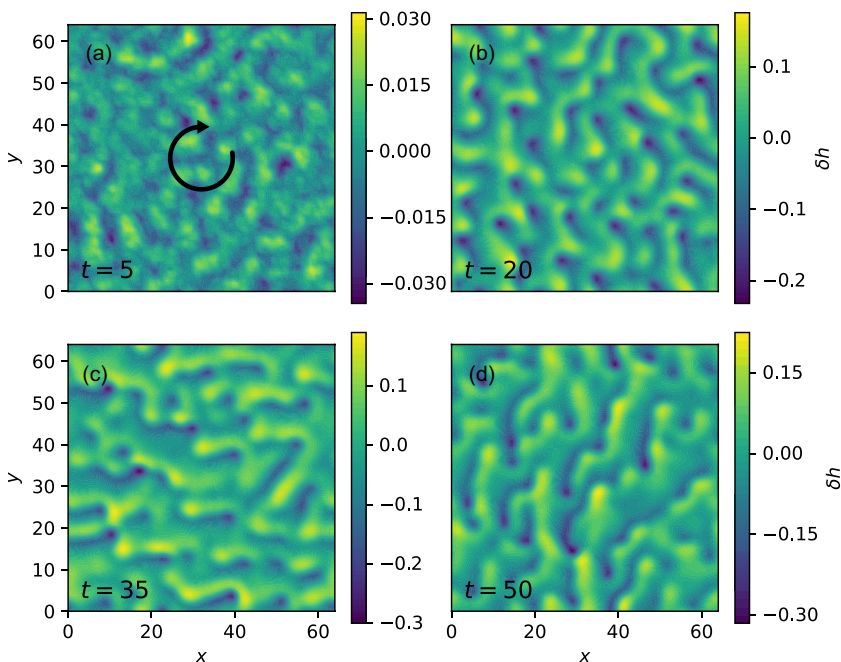

FIG. 7. Contour plots illustrating the height $h(x, y, t)$ of a 3D thin film, subjected to a rotating shear force with strength $B = 30$ and angular frequency $\Omega = 3\pi/32$ in the direction of the arrow in panel (a), as a function of time, with $Q = 10^{-2}$ and $h_0 = 1$. The color represents the deviation $\delta h(x, y) = h(x, y) - h_0$ from the initial film thickness h_0.
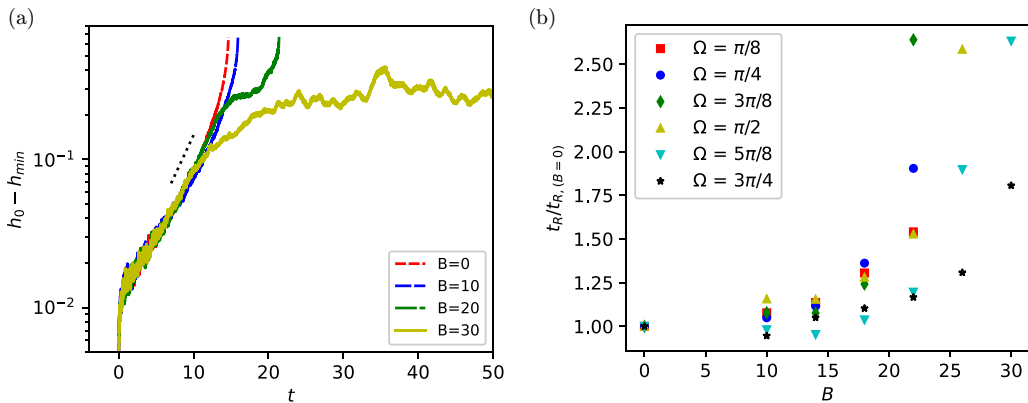
FIG. 8. (a) Time evolution of the height perturbation $h_0 - h_{\min}(t)$ for different values of the shear parameter B and angular frequency $\Omega = \pi/8$, in 3D solutions with rotating shear for $Q = 10^{-2}$. The dotted black line line indicates exponential behavior with a growth rate given by Eq. (9) and an arbitrary amplitude. (b) Rupture time t_R as a function of dimensionless shear stress B, for various angular frequencies Ω.

For a given angular frequency, Ω, the change in rupture time as B is increased, as depicted in Fig. 8, is actually quite similar to the 2D case of Sec. III A. For $B < 10$, shear does not significantly delay rupture, but does so once $B \gtrsim 15$ due to slower growth in the nonlinear regime. The critical value of B required is significantly higher than that observed in 2D, and varies with Ω. As seen in Fig. 8(b), it seems that the rupture-delaying effect of shear is strongest when $\Omega \approx 3\pi/4$. For lower frequencies, the shear suppresses rupture in one direction, but does not change fast enough to suppress it in the other, whereas for high frequencies, the shear does not remain in one direction for long enough to suppress rupture in that direction.

C. Implications for polymer processing

Let us now discuss the implications of the numerical results obtained above in a practical context. We specifically consider a polymer processing method: nanolayer coextrusion. This innovative process is based on a series of layer multiplying elements (LME) which apply the baker's transformation (successive slicing and recombining) to a stratified polymer melt flow to achieve multilayer systems, made of up to thousands of alternating layers of two or more polymers, each having nanometric thicknesses [48]. Many polymer pairs have been processed this way, whether glassy or semicrystalline, miscible or immiscible and in most cases stable, continuous and regular layers with thicknesses below 50 nm have been obtained [49–51]. We now use the results from Sec. III to investigate the physical case of nanolayer coextrusion, for which the values of physical parameters were specified in Sec. II A. Using Eq. (13) and putting back dimensions, the rupture time without shear for a layer having an initial thickness of 20 nm ($h_0 \approx 1.1$) would be in the 5–10 s range, hence much less than the typical processing time, between 1 and 2 min [42]. The stabilizing effect of shear could explain the stability of nanometric layers (around 20 nm), as already discussed in Ref. [35]. Looking at the 2D case [Fig. 4(c)], a significant increase of the rupture time occurs when B is higher than the critical value around 12.5, corresponding to a shear rate in the order of 20–25 s^{-1}, that is easily reached in classical extrusion conditions [42]. However, the novel 3D computations of the present study in uniaxial shear suggest that the shear force, B, has in fact a limited influence on the rupture time, which appears to contradict the previous conclusions drawn in 2D. The following hypotheses can be made concerning processing, especially nanolayer coextrusion: the minimal thickness achieved after the LMEs is actually higher than the one discussed previously, nanometric thicknesses being only reached after the LMEs when the flow goes through the flat sheet die, where the channel flow is shaped into a film having the desired width

and thickness. As the rupture timescales with the thickness to the power of 5, rupture may only occur when the polymer flow passes through this flat die, where the layer thickness reaches values below 100 nm. Interestingly, in the flat die, there is not only unidirectional shear but also a diverging radial flow, which may result in a more stabilizing situation as suggested by results presented in Figs. 7 and 8. Besides, we stress that the effect of elongation has not been elucidated yet, and we shall also mention that the boundary conditions used here in a single layer differ quite substantially with those occurring in a multilayer flow [52].

Finally, we comment on the 3D surface profiles showing the appearance of ridge-like and valley-like features aligned along the shear direction prior to rupture. This pattern formation is reminiscent of the experimental observations by Dmochowska *et al.* [36], where a PS thin film sandwiched between two PMMA thicker layers was dewetted under shear. Though this study focused on the dewetting kinetics, i.e., the hole growth after hole formation, it was observed that the dewetting holes take ellipsoidal shapes aligned with the local shear directions, contrary to the no-shear case [53,54]. The hole growth was accelerated in the shear direction while it remained similar to the no-shear case (with a slight increase caused by shear-thinning of the PMMA matrix) in the perpendicular direction.

IV. CONCLUSION

In this work, we have described how thermal fluctuations and shear affect the stability of thin nanometric films described by the thin film equation. Finite-element numerical solutions of the latter show that the role of the fluctuations is essentially to initiate perturbations of a characteristic size that is proportional to the thermal roughness of the interface. At later times, thermal fluctuations do not play a significant role in the dynamics of thin film rupture. By using a linear stability analysis, we give a rather simple prediction for the rupture time of a thin film as a function of initial height and temperature, in the absence of shear. When a shear force is introduced to a 2D system, rupture can be suppressed, resulting in the formation of a permanent traveling wave, while the initial size of the perturbations seems unaffected in the parameter range explored by the numerical solutions. In the more physically realistic case of unidirectional shear in 3D films rupture is not suppressed, as cross-shear perturbations grow unimpeded. Our results may explain why the reported rupture-inhibiting effect of shear has not been reported experimentally. This may be relevant in physical processes such as the thin air film formed below a droplet as it impacts on a surface, for which rupture is observed despite a high shear rate [55]. Our solutions do indicate, however, that rupture can be delayed if the direction of shear varies sufficiently rapidly with time—a situation of potential practical relevance for dewetting experiments and nanocoextrusion processes.

APPENDIX A: ADAPTIVE TIME-STEP SOLUTIONS

As described in Sec. II B, we stop our numerical solutions when the minimum height of the film reaches a threshold value of $h^* = 0.33$, and define the time at which this occurs as the rupture time of the film, t_R. Our justification for this is that the late stage of rupture is an almost instantaneous event that follows the power law described by Zhang and Lister [14]. To confirm that this is indeed a good assumption, we have computed numerical solutions as described in Sec. II B, but with an adaptive time step that decreases as the film height decreases, as well as a reduced grid spacing of
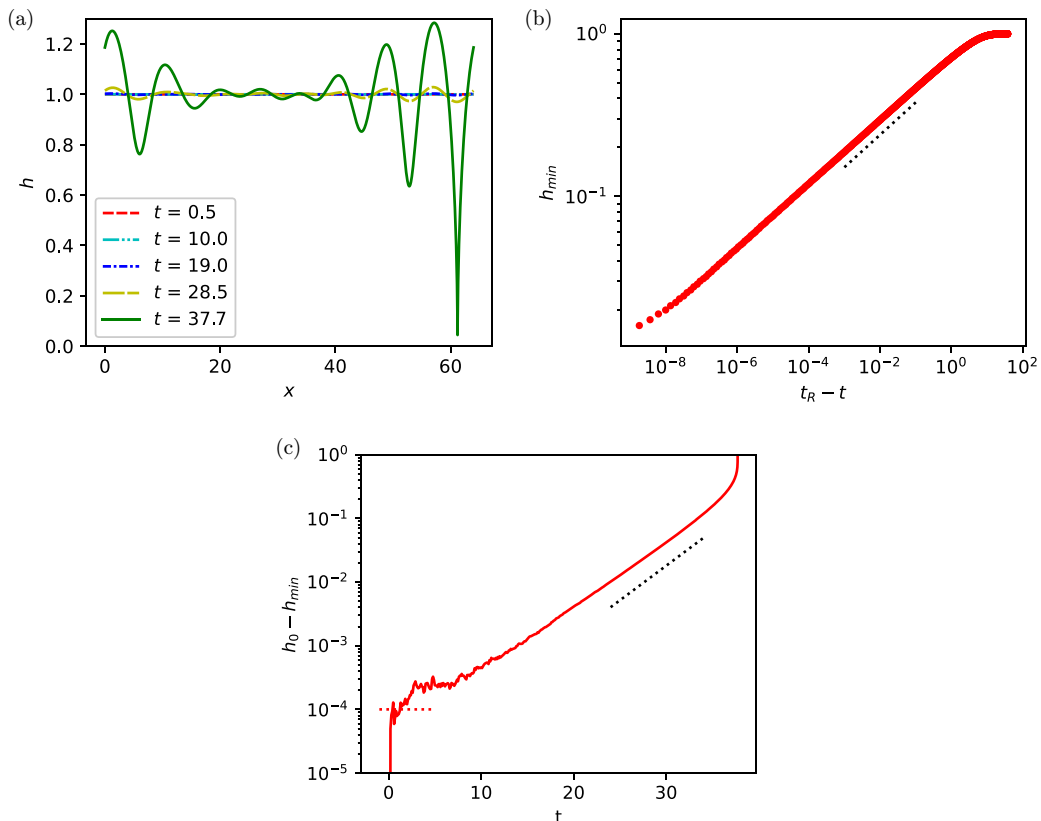
FIG. 9. (a) Film profiles at various times for numerical solutions using an adaptive time step for $Q = 0.0001$, $B = 0$, and $h_0 = 1$. (b) Minimum film height h_{min} as a function of the reverse time $t_R - t$, in log-log scale. The $(t_R - t)^{1/5}$ power law [14] with arbitrary prefactor is indicated by the dotted black line. (c) Amplitude of the height perturbation as a function of time. The dotted black line line indicates exponential behavior with a growth rate given by Eq. (9) and an arbitrary amplitude. The dotted red line indicates the Q value.

$\Delta x = 0.001$ to resolve the flow details in this regime. Figure 9 shows the results of such solutions. It is clear here that the late stage of rupture is accurately described by the aforementioned power law. The time elapsed between $h_{min} = 0.33$ and $h_{min} = 0.015$ is less than 0.1, which is a negligible fraction of the rupture time t_R, for all the cases simulated in this article. The results when shear is included are similar.

APPENDIX B: THERMAL ROUGHNESS OF A FLAT INTERFACE WITH SHEAR

In Sec. III A, we find that shear does not significantly change the initial size of the perturbations that lead to thin film rupture when thermal fluctuations are imposed. This is rather surprising in light of previous works which show that imposing a shear force significantly decreases the equilibrium thermal roughness of interfaces in other geometries [30,31]. We thus simulate a 2D thin film subjected to thermal fluctuations and shear but no disjoining pressure, for which the interface fluctuates around its initial height h_0 indefinitely. We then compute the thermal roughness of the interface at each time step as $\sigma = [\sum_{n=1}^{N}(h - h_0)^2/N]^{1/2}$, where n represents each of N total gridpoints. In Fig. 10(a) we show how σ varies in time when there is no shear. In both cases, σ fluctuates around a mean value of around $\sqrt{2}Q$ as expected due to the definition of Q in Sec. II A.
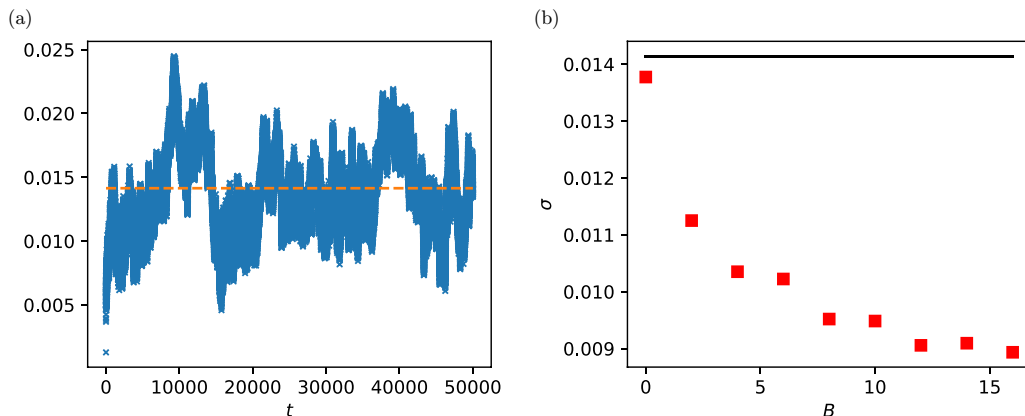
(a)

(b)

FIG. 10. (a) Instantaneous measured thermal roughness σ as a function of time for a numerical solution of a flat film without disjoining pressure with $Q = 0.01$, $h_0 = 1.0$, and $B = 0$. The dotted orange line shows the expected thermal roughness of $\sqrt{2}Q$. (b) The thermal roughness as a function of the dimensionless shear force B for $Q = 0.01$ and $h_0 = 1.0$. The black line shows the value of $\sqrt{2}Q$.

When we impose a shear $B \neq 0$ to the interface, we do indeed observe a decrease in the thermal roughness, as is shown in Fig. 10(b). In fact, for $B > 3$, σ is reduced by more than half. Although consistent with what we expect from the literature, this result seems to conflict with the results in Fig. 3(d) where the initial perturbation size is independent of B. Upon deeper reflection, however, it is not obvious that the equilibrium thermal roughness observed over time is the same as the size of instantaneous fluctuations. In our simulations of film rupture with both fluctuations and shear, it seems that perturbations to a flat film of size approximately Q are created during the first few timesteps before the disjoining pressure or shear have any effect. The sinusoidal perturbations that lead to rupture then form before the shear effect on thermal roughness has had any effect. It is thus important to distinguish between the time-averaged equilibrium effect of fluctuations and their instantaneous impact on the film.

[1] H. Wong, I. Fatt, and C. Radke, Deposition and thinning of the human tear film, J. Colloid Interface Sci. **184**, 44 (1996).

[2] V. Chandran Suja, A. Verma, E. Mossige, K. Cui, V. Xia, Y. Zhang, D. Sinha, S. Joslin, and G. Fuller, Dewetting characteristics of contact lenses coated with wetting agents, J. Colloid Interface Sci. **614**, 24 (2022).

[3] Z. Li, A. Olah, and E. Baer, Micro- and nano-layered processing of new polymeric systems, Prog. Polym. Sci. **102**, 101210 (2020).

[4] A. Bironeau, T. Salez, G. Miquelard-Garnier, and C. Sollogoub, Existence of a critical layer thickness in PS/PMMA nanolayered films, Macromolecules **50**, 4064 (2017).

[5] R. V. Craster and O. K. Matar, Dynamics and stability of thin liquid films, Rev. Mod. Phys. **81**, 1131 (2009).

[6] N. Ferrell and D. Hansford, Fabrication of micro- and nanoscale polymer structures by soft lithography and spin dewetting, Macromol. Rapid Commun. **28**, 966 (2007).

[7] P. Dhara, N. Bhandaru, A. Das, and R. Mukherjee, Transition from spin dewetting to continuous film in spin coating of liquid crystal 5CB, Sci. Rep. **8**, 7169 (2018).

[8] A. Vrij, Possible mechanism for the spontaneous rupture of thin, free liquid films, Discuss. Faraday Soc. **42**, 23 (1966).

[9] A. Sheludko, Thin liquid films, Adv. Colloid Interface Sci. **1**, 391 (1967).

[10] E. Ruckenstein and R. K. Jain, Spontaneous rupture of thin liquid films, J. Chem. Soc., Faraday Trans. 2 **70**, 132 (1974).

[11] M. B. Williams and S. H. Davis, Nonlinear theory of film rupture, J. Colloid Interface Sci. **90**, 220 (1982).

[12] A. Oron, S. Davis, and S. Bankoff, Long-scale evolution of thin liquid films, Rev. Mod. Phys. **69**, 931 (1997).

[13] A. Sharma and E. Ruckenstein, An analytical nonlinear theory of thin film rupture and its application to wetting films, J. Colloid Interface Sci. **113**, 456 (1986).

[14] W. W. Zhang and J. R. Lister, Similarity solutions for van der Waals rupture of a thin film on a solid substrate, Phys. Fluids **11**, 2454 (1999).

[15] M. C. Dallaston, M. A. Fontelos, D. Tseluiko, and S. Kalliadasis, Discrete self-similarity in interfacial hydrodynamics and the formation of iterated structures, Phys. Rev. Lett. **120**, 034505 (2018).

[16] A. Carlson and L. Mahadevan, Protein mediated membrane adhesion, Phys. Fluids **27**, 051901 (2015).

[17] J. Becker, G. Grün, R. Seemann, H. Mantz, K. Jacobs, K. R. Mecke, and R. Blossey, Complex dewetting scenarios captured by thin-film models, Nat. Mater. **2**, 59 (2003).

[18] K. Jacobs, R. Seemann, and S. Herminghaus, Stability and dewetting of thin liquid films, Polymer Thin Films **1**, 243 (2008).

[19] B. Davidovitch, E. Moro, and H. A. Stone, Spreading of viscous fluid drops on a solid substrate assisted by thermal fluctuations, Phys. Rev. Lett. **95**, 244505 (2005).

[20] G. Grün, K. Mecke, and M. Rauscher, Thin-film flow influenced by thermal noise, J. Stat. Phys. **122**, 1261 (2006).

[21] A. Carlson, Fluctuation assisted spreading of a fluid filled elastic blister, J. Fluid Mech. **846**, 1076 (2018).

[22] C. Pedersen, J. F. Niven, T. Salez, K. Dalnoki-Veress, and A. Carlson, Asymptotic regimes in elastohydrodynamic and stochastic leveling on a viscous film, Phys. Rev. Fluids **4**, 124003 (2019).

[23] S. Marbach, D. S. Dean, and L. Bocquet, Transport and dispersion across wiggling nanopores, Nat. Phys. **14**, 1108 (2018).

[24] J. A. Diez, A. G. González, and R. Fernández, Metallic-thin-film instability with spatially correlated thermal noise, Phys. Rev. E **93**, 013120 (2016).

[25] S. Nesic, R. Cuerno, E. Moro, and L. Kondic, Fully nonlinear dynamics of stochastic thin-film dewetting, Phys. Rev. E **92**, 061002(R) (2015).

[26] K. Mecke and M. Rauscher, On thermal fluctuations in thin film flow, J. Phys.: Condens. Matter **17**, S3515 (2005).

[27] M. A. Durán-Olivencia, R. S. Gvalani, S. Kalliadasis, and G. A. Pavliotis, Instability, rupture and fluctuations in thin liquid films: Theory and computations, J. Stat. Phys. **174**, 579 (2019).

[28] M. Shah, V. Steijn, C. Kleijn, and M. Kreutzer, Thermal fluctuations in capillary thinning of thin liquid films, J. Fluid Mech. **876**, 1090 (2019).

[29] C. Zhao, J. Liu, D. A. Lockerby, and J. E. Sprittles, Fluctuation-driven dynamics in nanoscale thin-film flows: Physical insights from numerical investigations, Phys. Rev. Fluids **7**, 024203 (2022).

[30] D. Derks, D. G. A. L. Aarts, D. Bonn, H. N. W. Lekkerkerker, and A. Imhof, Suppression of thermally excited capillary waves by shear flow, Phys. Rev. Lett. **97**, 038301 (2006).

[31] M. Thiébaud and T. Bickel, Nonequilibrium fluctuations of an interface under shear, Phys. Rev. E **81**, 031602 (2010).

[32] B. Bresson, C. Brun, X. Buet, Y. Chen, M. Ciccotti, J. Gâteau, G. Jasion, M. N. Petrovich, F. Poletti, D. J. Richardson, S. R. Sandoghchi, G. Tessier, B. Tyukodi, and D. Vandembroucq, Anisotropic superattenuation of capillary waves on driven glass interfaces, Phys. Rev. Lett. **119**, 235501 (2017).

[33] S. Kalpathy, L. Francis, and S. Kumar, Shear-induced suppression of rupture in two-layer thin liquid films, J. Colloid Interface Sci. **348**, 271 (2010).

[34] M. J. Davis, M. B. Gratton, and S. H. Davis, Suppressing van der Waals driven rupture through shear, J. Fluid Mech. **661**, 522 (2010).

[35] K. Kadri, J. Peixinho, T. Salez, G. Miquelard-Garnier, and C. Sollogoub, Dewetting of a thin polymer film under shear, Polymer **235**, 124283 (2021).

[36] A. Dmochowska, J. Peixinho, C. Sollogoub, and G. Miquelard-Garnier, Dewetting dynamics of sheared thin polymer films: An experimental study, ACS Macro Lett. **11**, 422 (2022).

[37] G. K. Batchelor, *An Introduction to Fluid Dynamics*, Cambridge Mathematical Library (Cambridge University Press, Cambridge, UK, 2000).

[38] Y. Zhang, J. E. Sprittles, and D. A. Lockerby, Nanoscale thin-film flows with thermal fluctuations and slip, Phys. Rev. E **102**, 053105 (2020).

[39] J. N. Israelachvili, *Intermolecular and Surface Forces*, 3rd ed. (Academic Press, San Diego, CA, 2011), pp. 253–289.

[40] S. Wu, Surface and interfacial tensions of polymer melts. II. Poly(methyl methacrylate), poly(n-butyl methacrylate), and polystyrene, J. Phys. Chem. **74**, 632 (1970).

[41] J. P. de Silva, F. Cousin, A. R. Wildes, M. Geoghegan, and M. Sferrazza, Symmetric and asymmetric instability of buried polymer interfaces, Phys. Rev. E **86**, 032801 (2012).

[42] A. Bironeau, Films multinanocouches de polymères amorphes coextrudés: élaboration, caractérisation et stabilité des nanocouches, Ph.D. thesis, ENSAM, 2016.

[43] A. Logg, K.-A. Mardal, G. N. Wells *et al.*, *Automated Solution of Differential Equations by the Finite Element Method*, edited by A. Logg, K.-A. Mardal, and G. N. Wells (Springer, Berlin, 2012).

[44] T. Oliphant, *Guide to NumPy* (MIT, Cambridge, MA, 2006).

[45] D. Moreno-Boza, A. Martínez-Calvo, and A. Sevilla, Stokes theory of thin-film rupture, Phys. Rev. Fluids **5**, 014002 (2020).

[46] J. E. Sprittles, J. Liu, D. A. Lockerby, and T. Grafke, Rogue nanowaves: A route to film rupture, Phys. Rev. Fluids **8**, L092001 (2023).

[47] See Supplemental Material at http://link.aps.org/supplemental/10.1103/PhysRevFluids.9.024201 for the videos of the 3D simulations.

[48] F. Gholami, L. Pakzad, and E. Behzadfar, Morphological, interfacial and rheological properties in multilayer polymers: A review, Polymer **208**, 122950 (2020).

[49] B. Rijal, L. Delbreilh, C. Sollogoub, E. Baer, and A. Saiter-Fourcin, Multiscale analysis of segmental relaxation in PC/PETg multilayers: Evidence of immiscible nanodroplets, Macromolecules **55**, 6562 (2022).

[50] Q. Lozay, Q. Beuguel, N. Follain, L. Lebrun, A. Guinault, G. Miquelard-Garnier, S. Tencé-Girault, C. Sollogoub, E. Dargent, and S. Marais, Structural and barrier properties of compatibilized PE/PA6 multinanolayer films, Membranes **11**, 75 (2021).

[51] S. F. Nassar, S. Domenek, A. Guinault, G. Stoclet, N. Delpouve, and C. Sollogoub, Structural and dynamic heterogeneity in the amorphous phase of poly (l, l-lactide) confined at the nanoscale by the coextrusion process, Macromolecules **51**, 128 (2018).

[52] R. D. Lenz and S. Kumar, Instability of confined thin liquid film trilayers, J. Colloid Interface Sci. **316**, 660 (2007).

[53] Y. Zhu, A. Bironeau, F. Restagno, C. Sollogoub, and G. Miquelard-Garnier, Kinetics of thin polymer film rupture: Model experiments for a better understanding of layer breakups in the multilayer coextrusion process, Polymer **90**, 156 (2016).

[54] M. S. Chebil, J. D. McGraw, T. Salez, C. Sollogoub, and G. Miquelard-Garnier, Influence of outer-layer finite-size effects on the dewetting dynamics of a thin polymer film embedded in an immiscible matrix, Soft Matter **14**, 6256 (2018).

[55] J. M. Kolinski, S. M. Rubinstein, S. Mandre, M. P. Brenner, D. A. Weitz, and L. Mahadevan, Skating on a film of air: Drops impacting on a surface, Phys. Rev. Lett. **108**, 074503 (2012).